RESEARCH ARTICLE

Reynolds-Number-Dependent Energy Harvesting by Freely Rotating Variable-angle Rhombic and Variable-side-length Parallelogram Cylinders

Ruiyong Mou[1,2,*], **Xingrong Huang**[3] **and Feng Liu**[4]

[1] Research Institute of Aero-Engine, Beihang University, Beijing 100191, China
[2] BCC Lab, Hangzhou International Innovation Institute of Beihang University, Hangzhou 311115, China
[3] Sino-French Carbon Neutrality Research Center, Ecole Centrale de Pékin, Beihang University, Beijing 100191, China
[4] School of Energy and Power Engineering, North University of China, Taiyuan 030051, China

Abstract

Bluff-body flow-energy harvesters are commonly designed around translational vibration, whereas freely rotating polygonal sections provide an alternative route that harnesses rotational oscillations. In this study, Reynolds-number-dependent energy-harvesting responses of two reconfigurable sections, a variable-angle rhombic cylinder and a variable-side-length parallelogram cylinder, are investigated using an immersed boundary method. The body rotates freely about its centroid without a linear spring or external damping. Results show that at $Re = 40$, decreasing the rhombus angle improves start-up and increases the bounded-oscillation amplitude, favoring oscillation-based harvesting, while the parallelogram oscillation amplitude varies non-monotonically with side-length ratio, with $\lambda = 1.1$ yielding the largest bounded-oscillation amplitude. At $Re = 150$, acute rhombi sustain the largest bounded oscillations, whereas the square cylinder develops autorotation and favors rotary harvesting; the parallelogram family remains on bounded oscillatory branches, with $\lambda = 1.5$ producing the largest response envelope. Phase-resolved analyses reveal that periodic near-wake reorganization maintains the oscillation of acute rhombi through favorable alignment between the hydrodynamic moment and the angular velocity. These findings provide geometry-selection guidelines for oscillatory and rotary flow-energy harvesters.

Keywords: energy harvesting, vortex-induced rotation, immersed boundary method, variable-angle rhombic cylinder, variable-side-length parallelogram cylinder.

1 Introduction

Harvesting energy from ambient flows has become an important route toward self-powered sensing,

Submitted: 24 July 2026
Revised: 16 September 2026
Accepted: 23 September 2026
Published: 29 September 2026

Vol. 1, **No.** 2, 2026.
10.62762/JCN.2026.692457

***Corresponding author:**
✉ Ruiyong Mou
by2032116@buaa.edu.cn

Citation
Mou, R., Huang, X., & Liu, F. (2026). Reynolds-Number-Dependent Energy Harvesting by Freely Rotating Variable-angle Rhombic and Variable-side-length Parallelogram Cylinders. *Journal of Carbon Neutrality*, 1(2), 155–166.

© 2026 by the Authors. Published by Institute of Central Computation and Knowledge. This is an open access article under the CC BY license (https://creativecommons.org/licenses/by/4.0/).

distributed monitoring, and small autonomous systems operating where battery replacement is difficult or uneconomical. Within this broader context, flow-induced-motion devices are attractive because they extract usable motion from wake instability rather than from high tip-speed rotary machinery. Recent reviews have shown that the relevant mechanisms include vortex-induced vibration (VIV), galloping, flutter, buffeting, and a smaller class of rotation-type responses, with performance governed jointly by body geometry, structural dynamics, and power-take-off design [1, 2]. These attributes make flow-energy harvesters a promising low-carbon complement to conventional power sources for distributed sensing and remote monitoring, directly supporting carbon-neutral energy systems by reducing dependence on battery-based or grid-connected power supplies.

That role of geometry is well established for oscillation-based harvesters, and the translational-vibration literature provides the clearest reference point for comparison with the rotational responses examined here. Studies of transverse galloping and related bluff-body devices have shown that cross-sectional shape strongly affects galloping onset velocity and stability [3–5], response amplitude, synchronization range, and conversion efficiency [6–10], with structural parameters such as damping ratio and mass ratio further modulating the harvested power for a given geometry [11]. The emerging physical picture is that geometry does not merely rescale the force level; it reorganizes shear-layer deflection, near-wake topology, and the phase relation between motion and fluid loading [9, 10]. However, most devices in this class are formulated around translational motion, typically the cross-flow oscillation of a spring-mounted body, so the geometric effect is usually intertwined with an imposed linear restoring force and an externally prescribed damping level.

In parallel, the fluid-mechanics literature has developed a substantial understanding of vortex-induced rotation (VIR) and other free-rotation responses of rigid bodies. Freely rotating elliptic, triangular, rectangular, and square sections have all been studied, revealing stable equilibria, bounded oscillations, reverse rotation, random rotation, and autorotation, together with the corresponding torque-generation mechanisms and analytical models thereof [12–20]. Mou *et al.* [20] showed that even the square cylinder possesses a rich response map when Reynolds number and density ratio are varied. Yet these studies were mainly posed as canonical fluid–structure-interaction problems, rather than as geometry-selection problems for harvesting-oriented rotating units.

Viewed from the energy-harvesting side, the unresolved issue is not simply which VIR regimes exist, but how geometry selects among bounded oscillation, intermittent reversal, and persistent one-way rotation, and which wake states are responsible for these different outputs. This viewpoint also motivates the simplified structural model adopted here. The body is not attached to a linear spring and no external damper is introduced. The purpose is to isolate the hydrodynamic moment generated by geometric reconfiguration itself, so that the intrinsic rotational tendency of the section can be identified before additional restoring or dissipative parameters associated with a specific power-take-off model are imposed. Although torsional-galloping and other rotation-based harvesting concepts have been discussed in the literature [1, 21, 22], systematic analysis of freely rotating, geometry-adjustable polygonal sections from this perspective remains limited.

The present work addresses this issue through two minimal families of reconfigurable polygonal sections: a variable-angle rhombus and a variable-side-length parallelogram. The rhombic family, parameterized by the acute angle α, varies the corner sharpness continuously from the square limit to increasingly slender diamond-like shapes; the parallelogram family, constructed at fixed $\alpha = \pi/4$ with adjustable side-length ratio $\lambda = L/L_0$, isolates the effect of elongation at fixed obliqueness. These two families separate two distinct geometric controls on rotational dynamics—corner angle and side-length asymmetry—and therefore provide a convenient setting for examining how geometry modifies near-wake vortices, and changes the phase relation among rotation angle θ, angular velocity ω, and hydrodynamic moment coefficient C_m. In this sense, the problem is posed as a fluid-mechanical study of torque-producing wake structures relevant to rotational energy extraction, rather than as a further catalog of bluff-body response modes.

Guided by the design objective of adaptive rotational harvesting sections, the study focuses on two representative Reynolds numbers, $Re = 40$ and 150, with density ratio fixed at 2. The lower Reynolds

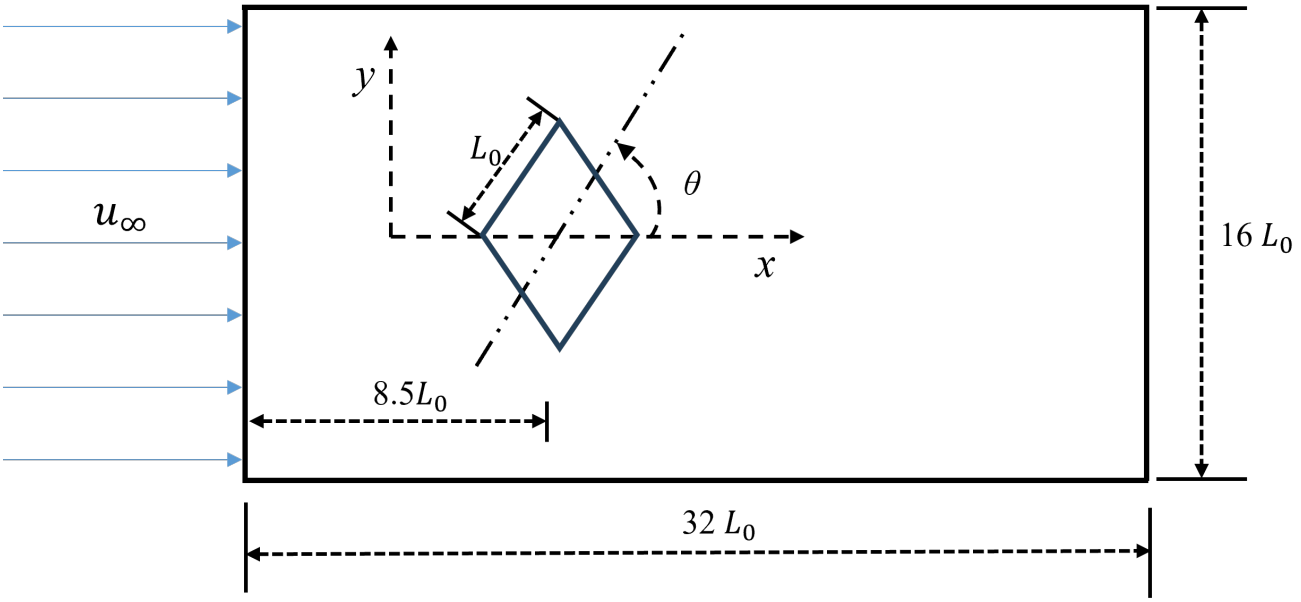

Figure 1. Computational domain and geometry families considered in the present study. This sketch shows the centroid-fixed, freely rotatable section placed in a $32L_0 \times 16L_0$ domain.

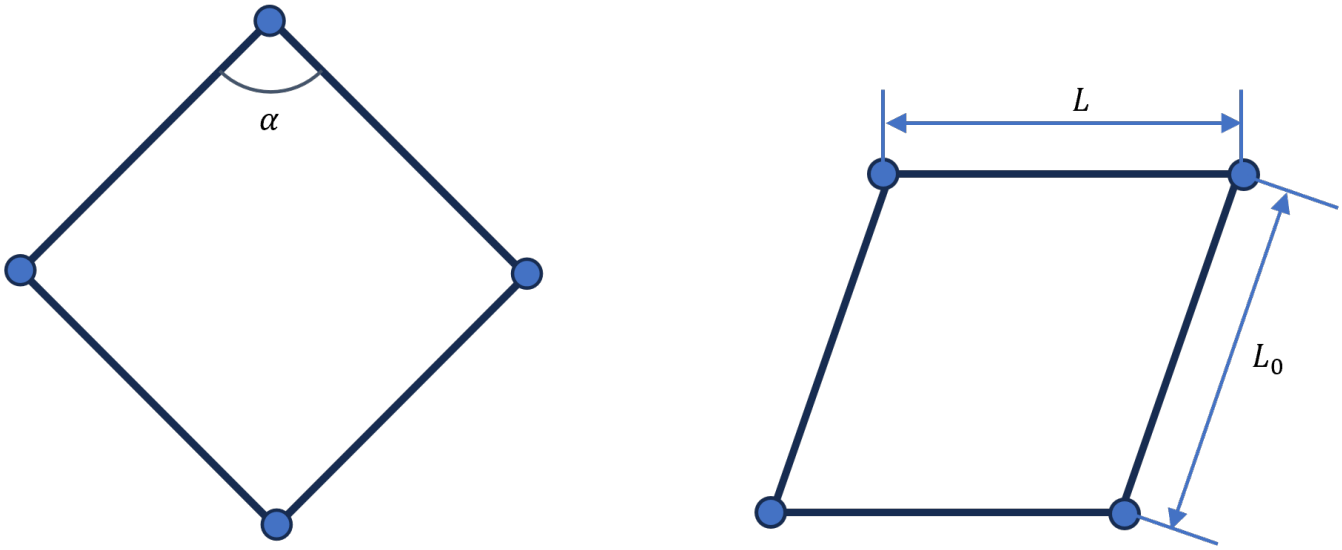

Figure 2. Schematic definitions of the two reconfigurable geometry families. The left panel shows the variable-angle rhombic family, and the right panel shows the variable-side-length parallelogram family.

number is used to assess low-speed start-up and bounded oscillation, whereas the higher Reynolds number is used to assess whether the same geometry sustains large oscillations or develops autorotation. For the rhombic family, four angles are examined, $\alpha = \pi/2$, $\pi/3$, $\pi/4$, and $\pi/6$; for the parallelogram family, three side-length ratios are considered, $\lambda = 1$, 1.5, and 2, at $\alpha = \pi/4$, supplemented at $Re = 40$ by a refined scan over $\lambda = 1.1$–1.4. Finally, phase-resolved analyses of the angle, angular velocity, moment, and wake vorticity are conducted to investigate the mechanism sustaining the oscillation of acute rhombi at low Reynolds numbers.

2 Problem description and numerical method

2.1 Geometry families and response metrics

We consider a two-dimensional incompressible cross-flow of free-stream speed u_∞ past a rigid polygonal cylinder whose centroid is fixed in space while rotation about the spanwise axis through the centroid is free. The structural system therefore has a single degree of freedom, namely the angle $\theta(t)$, as shown in Figure 1. No linear spring, structural damping, or prescribed power take-off is introduced, so that the rotational response is determined solely by the fluid-induced moment.

As shown in Figure 2, two families of reconfigurable sections are investigated, i.e., a variable-angle rhombic cylinder and a variable-side-length parallelogram cylinder. In the rhombic family, all sides are equal to L_0 and the interior angle is varied as

$$\alpha = \frac{\pi}{2},\ \frac{\pi}{3},\ \frac{\pi}{4},\ \frac{\pi}{6}. \tag{1}$$

The case $\alpha = \pi/2$ reduces to the square-cylinder limit and therefore connects directly to the literature on freely rotating square sections [15, 20]. In the parallelogram family, one side is fixed at L_0, the included angle is fixed at $\alpha = \pi/4$, and the adjacent side is varied as

$$L = \lambda L_0, \qquad \lambda = 1,\ 1.5,\ 2. \tag{2}$$

The case $\lambda = 1$ recovers the rhombus with $\alpha = \pi/4$. Figure 3 summarizes the two geometry families.

The Reynolds number is defined with the reference side length L_0,

$$Re = \frac{\rho_f u_\infty L_0}{\mu}, \tag{3}$$

where μ is the dynamic viscosity, u_∞ is the inflow velocity, L_0 is the reference side length (the side length of the rhombus, and the fixed side of the parallelogram), and ρ_f is the fluid density. Although these Reynolds numbers are lower than those in large-scale engineering flows, they are representative of small-scale flow-energy harvesting devices. For example, flow-induced rotation of polygonal prisms including triangular, square, and pentagonal cross-sections has been studied numerically at $Re = 100$ [23], and, for reference, an elastically mounted cylinder with mechanically coupled rotation at $Re = 100$ has achieved a maximum harvesting efficiency of 0.424 under a spring-constrained structural model, with the power in the galloping regime exceeding that in the VIV regime by more than 20 times [24], indicating that incorporating a rotational degree of freedom can substantially enhance energy conversion. In both cases the solid-to-fluid density ratio is fixed at

$$\rho_r = \frac{\rho_s}{\rho_f} = 2, \tag{4}$$

where ρ_s and ρ_f denote the solid and fluid densities, respectively.

A small initial angular perturbation is imposed to trigger motion, after which the section evolves only under the hydrodynamic torque. The harvesting potential of each geometry is assessed through response quantities that would directly affect a practical converter: the asymptotic angular amplitude and the long-term response regime (bounded oscillation or autorotation). For a bounded periodic state, the angular amplitude is defined as

$$A_\theta = \frac{\theta_{\max} - \theta_{\min}}{2}. \tag{5}$$

2.2 Governing equations and immersed-boundary formulation

The flow is governed by the incompressible Navier–Stokes equations,

$$\nabla \cdot \mathbf{u} = 0, \tag{6}$$

$$\rho_f \left(\frac{\partial \mathbf{u}}{\partial t} + \mathbf{u} \cdot \nabla \mathbf{u} \right) = -\nabla p + \mu \nabla^2 \mathbf{u} + \mathbf{f}, \tag{7}$$

where $\mathbf{u}$ is the fluid velocity, p is the hydrodynamic pressure, and $\mathbf{f}$ is the Eulerian forcing density used to impose the no-slip condition on the moving immersed boundary. The structural rotation satisfies the angular-momentum equation

$$I \frac{d^2\theta}{dt^2} = T, \tag{8}$$

where I is the mass moment of inertia per unit span, θ is the rotation angle (as shown in Figure 1), T is the hydrodynamic torque exerted by the fluid.

For the present geometry families, closed-form expressions for the moment of inertia can be obtained directly. Let a and b denote the two side lengths of a homogeneous parallelogram and let $A = ab\sin\alpha$ be its area. The centroidal moment of inertia about the spanwise axis is

$$I = \rho_s \int_A r^2\, dA = \rho_s A \frac{a^2 + b^2}{12}. \tag{9}$$

Accordingly, for the rhombic family ($a = b = L_0$),

$$I_{\mathrm{rh}} = \rho_s L_0^4 \frac{\sin\alpha}{6}, \tag{10}$$

and for the parallelogram family ($a = L_0,\ b = \lambda L_0$),

$$I_{\mathrm{pa}} = \rho_s L_0^4 \frac{\lambda(1+\lambda^2)\sin\alpha}{12}. \tag{11}$$

The geometry dependence of I is therefore retained explicitly rather than absorbed into a constant rotational inertia.

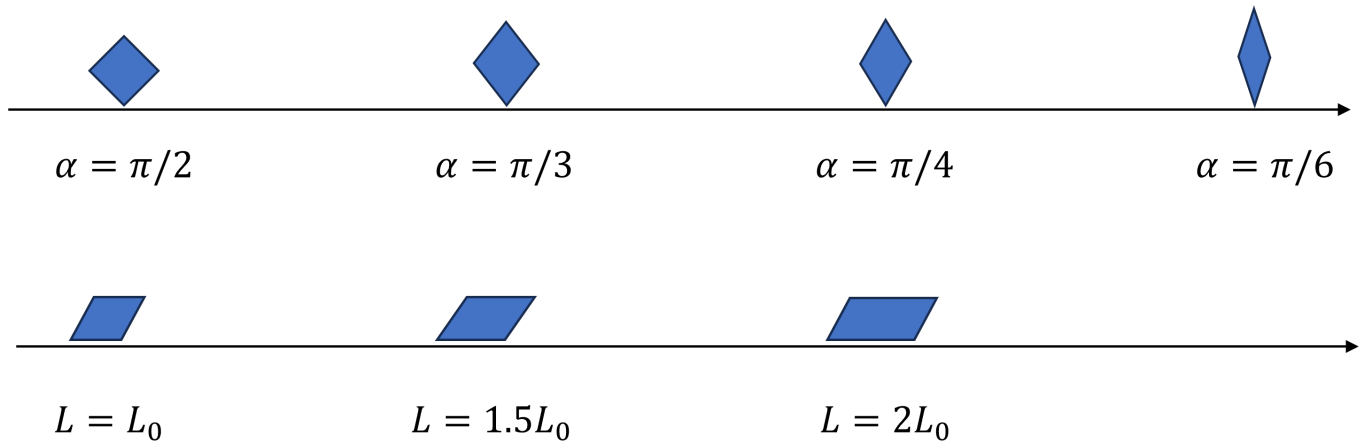

Figure 3. Parameter settings of the two geometry families considered in the present study. The upper row shows the rhombic cases with $\alpha = \pi/2, \pi/3, \pi/4$, and $\pi/6$, and the lower row shows the parallelogram cases with $\lambda = 1, 1.5$, and 2 at $\alpha = \pi/4$.

The hydrodynamic torque is evaluated from the immersed-boundary force distribution,

$$T = \int_{\Gamma_b} (\mathbf{r} \times \mathbf{F}) \cdot \mathbf{e}_z \, ds, \tag{12}$$

where Γ_b is the body contour, $\mathbf{r}$ is the position vector relative to the centroid, and $\mathbf{F}(s,t)$ is the Lagrangian boundary force density. Following the direct-forcing immersed-boundary framework introduced by Huang *et al.* [25] and later adopted by Mou *et al.* [20], the boundary force density $\mathbf{F}(s,t)$ and the interpolation and spreading operators are written as

$$\mathbf{F} = \kappa_1 \int_0^t (\mathbf{U}_{ib} - \mathbf{U}_s) \mathrm{d}t' - \kappa_2 (\mathbf{U}_{ib} - \mathbf{U}_s), \tag{13}$$

$$\mathbf{U}_{ib}(s,t) = \int_\Omega \mathbf{u}(\mathbf{x},t) \delta(\mathbf{X}(s,t) - \mathbf{x}) \mathrm{d}\mathbf{x}, \tag{14}$$

$$\mathbf{f}(\mathbf{x},t) = \int_{\Gamma_b} \mathbf{F}(s,t) \delta(\mathbf{x} - \mathbf{X}(s,t)) \mathrm{d}s, \tag{15}$$

where κ_1 and κ_2 are positive feedback coefficients (distinct from the geometric interior angle α defined above); Ω is the fluid domain; $\mathbf{X}(s,t)$ is the position of the Lagrangian point on the immersed boundary Γ_b; $\mathbf{U}_s$ is the Lagrangian velocity of the immersed boundary determined by the rigid-body rotation, i.e. $\mathbf{U}_s = \omega \, \mathbf{e}_z \times \mathbf{r}$; $\mathbf{U}_{ib}$ is the interpolated fluid velocity at the boundary; and δ is the Dirac delta function (a smoothed discrete delta function δ_h is used in the simulations).

Using L_0, u_∞, and ρ_f as reference scales, the dimensionless governing equations become

$$\frac{\partial \mathbf{u}^*}{\partial t^*} + \mathbf{u}^* \cdot \nabla^* \mathbf{u}^* = -\nabla^* p^* + \frac{1}{Re} \nabla^{*2} \mathbf{u}^* + \mathbf{f}^*, \tag{16}$$

$$I^* \frac{d^2\theta}{dt^{*2}} = T^*, \tag{17}$$

where $t^* = t\,u_\infty / L_0$, $I^* = I/(\rho_f L_0^4)$, $T^* = T/(\rho_f u_\infty^2 L_0^2)$, and $\omega^* = d\theta/dt^*$. The hydrodynamic moment coefficient is defined as

$$C_m = \frac{2T}{\rho_f u_\infty^2 L_0^2} = 2T^*. \tag{18}$$

2.3 Computational configuration and validation

The numerical configuration in this paper is kept consistent with that used by Mou *et al.* [20]. The computational domain measures $32L_0$ in the streamwise direction and $16L_0$ in the transverse direction. The section centroid is located $8.5L_0$ downstream of the inlet. Uniform inflow is imposed on the inlet boundary. The production simulations use the converged Cartesian grid reported in Table 1, together with the same time-marching protocol and immersed-boundary forcing parameters as in that reference.

Validation is carried out with the canonical benchmark of flow past a fixed square cylinder at $Re = 100$. Table 1 summarizes the domain- and grid-independence study, showing that the mean drag coefficient C_D, the root-mean-square lift coefficient $C_{L,\mathrm{rms}}$, and the Strouhal number St have converged when the grid number is 512×1024 and the computational domain is $32L_0 \times 16L_0$: refining the grid to 1024×2048 changes C_D and St by less than 1% (and $C_{L,\mathrm{rms}}$ by about 3.5%). Given that the present study focuses on rotational dynamics rather than precise lift statistics, and that C_D and St are converged to within 1%, the 512×1024 grid is deemed sufficient for the present parameter study.

Table 1. Domain and grid-independence study for the fixed square cylinder at $Re = 100$, following Mou *et al.* [20].

Domain	Grid	C_D	$C_{L,\mathrm{rms}}$	St
$8L_0 \times 8L_0$	256×256	2.3643	0.1705	0.1883
$8L_0 \times 16L_0$	256×512	1.8267	0.1906	0.1650
$32L_0 \times 16L_0$	512×1024	1.5874	0.1938	0.1477
$32L_0 \times 64L_0$	1024×2048	1.5084	0.1805	0.1409
$16L_0 \times 32L_0$	256×512	1.6585	0.1853	0.1433
$16L_0 \times 32L_0$	512×1024	1.5874	0.1938	0.1477
$16L_0 \times 32L_0$	1024×2048	1.5733	0.2006	0.1483

Table 2 compares the present benchmark values with representative literature data. The agreement is satisfactory and consistent with the reference implementation. In addition, Mou *et al.* [20] showed that the same solver reproduces the Reynolds-number sweep reported by Ryu and Iaccarino [15], with relative deviations below 4% in the drag and lift statistics over $45 \leq Re \leq 150$. Because the present study employs the same numerical framework and the same converged grid, that validation carries over directly.

Table 2. Comparison with published fixed-square-cylinder benchmarks at $Re = 100$.

Reference	C_D	$C_{L,\mathrm{rms}}$	St
Yoon et al. [26]	1.4385	0.1774	—
Sen et al. [27]	1.5287	0.1928	0.1452
Park et al. [28]	1.378	0.161	0.141
Ryu and Iaccarino [15]	1.5642	0.1932	0.1506
Present	1.5874	0.1938	0.1477

3 Results

The rotational responses of the two reconfigurable families—the variable-angle rhombic cylinder and the variable-side-length parallelogram cylinder—are now examined at the two Reynolds numbers. First, the low-Reynolds-number response at $Re = 40$ is analyzed, focusing on start-up and the maintenance of bounded oscillation under weak-flow conditions. Second, the behavior at $Re = 150$ is investigated, where the competition between bounded oscillation and self-rotation becomes central. Finally, the phase-resolved mechanism sustaining energetic bounded oscillation of acute rhombi is elucidated. In what follows, bounded oscillatory motion is interpreted as the kinematic regime relevant to oscillation-based energy harvesting, whereas a long-term monotonic angular drift is taken as the signature favorable to rotary harvesting.

3.1 Geometry dependence of low-Reynolds-number start-up and bounded oscillation

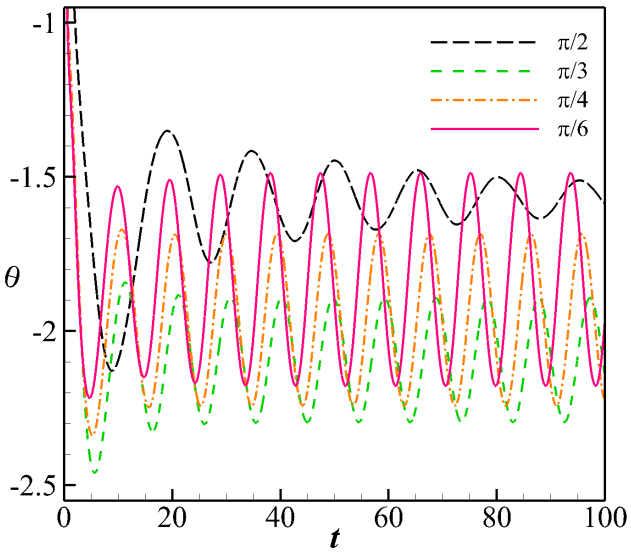

Figure 4. Time histories of the rotation angle for the variable-angle rhombic family at $Re = 40$, with interior angles $\alpha = \pi/2$, $\pi/3$, $\pi/4$, and $\pi/6$.

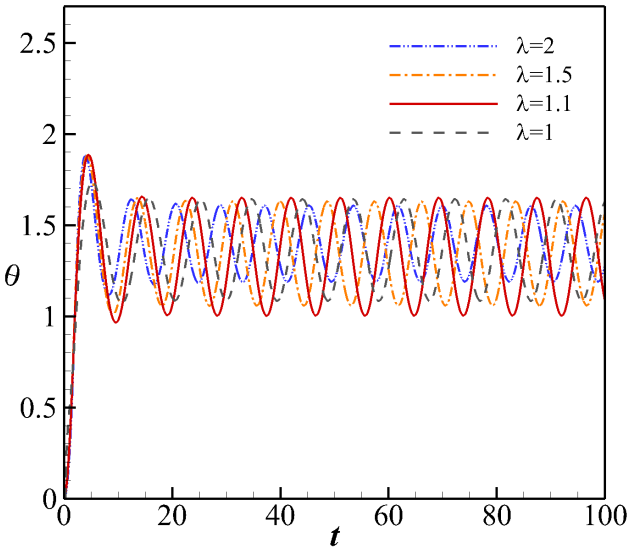

Figure 5. Time histories of the rotation angle for the variable-side-length parallelogram family at $Re = 40$, with side-length ratios $\lambda = 1$, 1.1, 1.5, and 2.

We first examine the cylinder response at low Reynolds number, focusing on start-up and the maintenance of bounded oscillation under weak inflow. Figure 4 shows the angle histories for the variable-angle rhombic family at $Re = 40$. For $\alpha = \pi/3$, $\pi/4$, and $\pi/6$, the angular responses follow a qualitatively similar pattern: after a short transient, each settles into a sustained oscillation about an equilibrium angle with a

stable amplitude. However, the oscillation amplitudes differ markedly: they increase monotonically with decreasing interior angle, with the largest amplitude for $\alpha = \pi/6$ and the smallest for $\alpha = \pi/3$. This trend confirms that a sharper rhombus (smaller α) enhances the oscillatory response, which is advantageous for oscillation-based energy harvesting.

Notably, when $\alpha = \pi/2$ the shape becomes a square, and its angular response is fundamentally different from that of the three acute rhombi. The oscillation amplitude of the square section decays continuously with time and does not approach a stable finite value. Mou *et al.* [20] have shown that, under these conditions, the amplitude ultimately decays to zero. Consequently, a square cylinder cannot sustain self-sustained oscillation at $Re = 40$, making it unsuitable for oscillation-based energy harvesting. In summary, at $Re = 40$ the square cylinder ($\alpha = \pi/2$) fails to start up, whereas the three acute rhombi ($\alpha = \pi/3, \pi/4, \pi/6$) successfully start up and sustain stable finite-amplitude oscillations.

We next examine the response of the parallelogram family at low Reynolds number, which differs markedly from that of the rhombic family. Figure 5 shows that, for all side-length ratios ($\lambda = 2, 1.5, 1.1, 1$), the cylinder starts up rapidly from the prescribed initial perturbation and settles into stable bounded oscillation about an equilibrium angle, confirming that every member of the family completes start-up successfully at $Re = 40$. The difference between the $\lambda = 1$ and $\lambda = 1.5$ cases is not obvious, as their amplitudes are close. To verify whether the true maximum lies between these two points, additional simulations were performed for $\lambda = 1.1$, 1.2, 1.3, and 1.4. The resulting variation of the bounded oscillation amplitude with λ is shown in Figure 6. The oscillation amplitude does not vary monotonically with the side-length ratio λ: the largest bounded amplitude occurs at an intermediate ratio near $\lambda = 1.1$, rather than at $\lambda = 1.5$, while both the $\lambda = 1$ and $\lambda = 2$ cases yield noticeably weaker oscillations (as shown in Figure 5). This indicates that, at a fixed obliqueness, the most favorable low-speed response is obtained not at the largest elongation but at a moderate degree of side-length asymmetry. Consequently, for oscillation-based energy harvesting employing a parallelogram cylinder, a moderate side-length ratio around $\lambda = 1.1$ should be adopted to maximize the oscillatory amplitude at $Re = 40$.

A comparison of the two geometry families at $Re = 40$ shows that, although both can sustain bounded motion at this low Reynolds number, they do so through fundamentally different geometric trends. For the rhombic family, the response is governed monotonically by corner sharpness, and the smallest angle considered here gives both the best start-up and the largest oscillation amplitude. For the parallelogram family, the response is optimized at an intermediate side-length ratio rather than at either limiting geometry. Taken together, the low-Reynolds-number results demonstrate that both start-up and the ability to sustain oscillation are strongly dependent on cross-sectional shape. From the perspective of oscillation-based energy harvesting, a smaller rhombus angle and the intermediate parallelogram with $\lambda = 1.1$ are therefore the preferred geometries under weak-flow conditions.

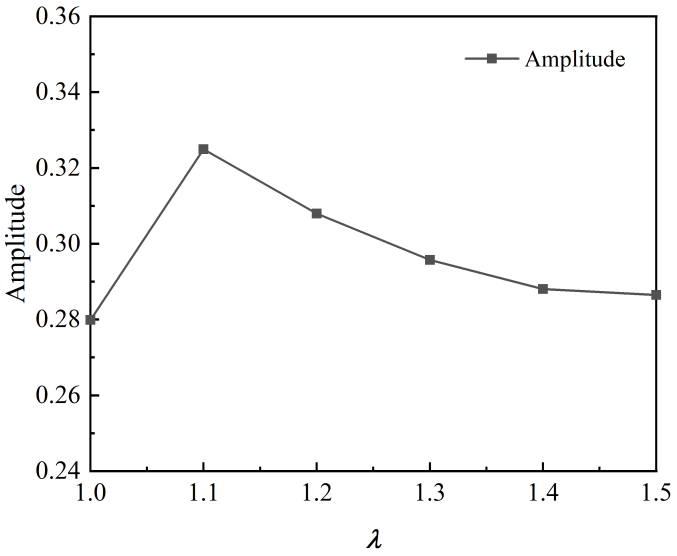

Figure 6. Variation of the bounded oscillation amplitude with the side-length ratio λ for the parallelogram family at $Re = 40$.

3.2 Geometry dependence of high-Reynolds-number bounded oscillation and self-rotation

We next examine the vortex-induced rotation of the rhombic family at $Re = 150$, focusing on how cross-sectional shape influences the transition in motion regime. The angle histories in Figure 7 confirm that the interior angle remains the dominant geometric parameter at $Re = 150$. For the three acute rhombi ($\alpha = \pi/3, \pi/4, \pi/6$), the responses follow a pattern similar to that at $Re = 40$: each starts from the initial perturbation and rapidly settles into stable bounded oscillation about an equilibrium angle. The oscillation amplitude increases monotonically with decreasing α,

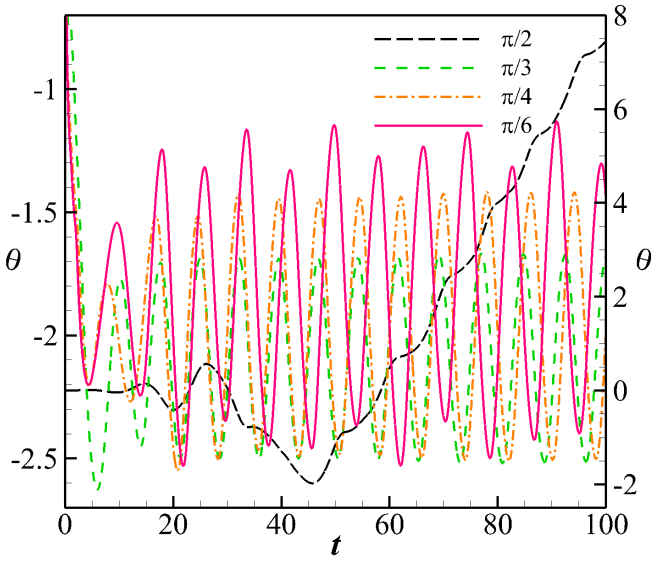

Figure 7. Time histories of the rotation angle for the variable-angle rhombic family at $Re = 150$, with interior angles $\alpha = \pi/2$, $\pi/3$, $\pi/4$, and $\pi/6$. The case $\alpha = \pi/2$ (black long-dashed line) is plotted against the right vertical axis, while all other cases are plotted against the left vertical axis.

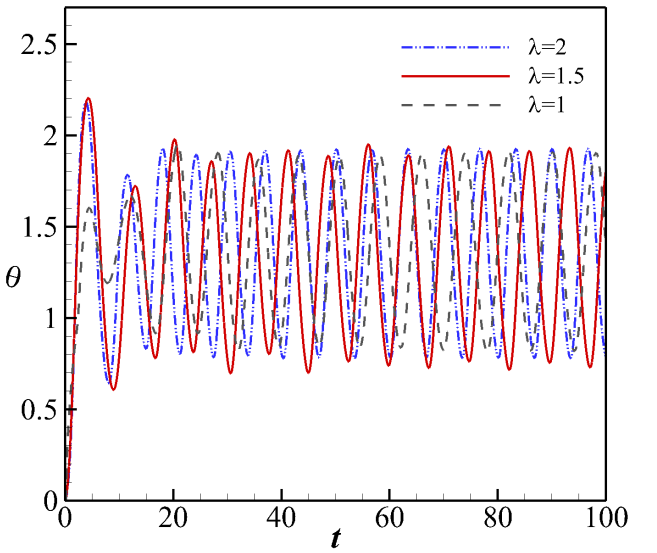

Figure 8. Time histories of the rotation angle for the variable-side-length parallelogram family at $Re = 150$, with side-length ratios $\lambda = 1$, 1.5, and 2.

being largest for $\alpha = \pi/6$ and smallest for $\alpha = \pi/3$, and the amplitudes are all noticeably larger than at $Re = 40$. Thus, reducing α continues to enhance the bounded oscillation at $Re = 150$, favoring oscillation-based harvesting.

In stark contrast, the square cylinder ($\alpha = \pi/2$) behaves fundamentally differently. After a brief initial transient, it does not oscillate about an equilibrium angle but instead rotates continuously in one direction, a state that Mou *et al.* [20] identified as the autorotation regime. For a rotary harvester, this continuous rotation delivers uninterrupted unidirectional angular motion, which is directly compatible with rotary generators.

In summary, at $Re = 150$, the optimal geometric choice within the rhombic family depends entirely on the intended harvesting mode. For oscillation-based harvesting, the interior angle should be made as small as possible to maximize the oscillation amplitude. For rotary harvesting, among the angles tested only the square section ($\alpha = \pi/2$) triggers continuous autorotation and is therefore the candidate for rotary energy extraction.

The parallelogram family behaves differently at $Re = 150$. As shown in Figure 8, all three parallelogram cylinders remain in bounded oscillation, and none develops autorotation under the conditions tested. The oscillation amplitudes are more similar than at $Re = 40$, showing a reduced sensitivity to λ once the wake is more energetic. The $\lambda = 1.5$ case yields the largest oscillation envelope. A plausible interpretation, offered as a hypothesis, is that this intermediate optimum reflects a balance between the effective aerodynamic moment arm and the separation/reattachment behavior of the body. As λ increases, the moment arm grows and tends to enhance the driving torque, but too large an elongation allows the separated shear layers to reattach or form a more stable near-wake, reducing the pressure asymmetry and increasing fluid damping. The optimum therefore occurs at a moderate elongation that preserves near-wake asymmetry while providing a sufficient moment arm. At lower Reynolds number the flow is less unsteady, so a smaller elongation already suffices; at higher Reynolds number a larger moment arm is needed for the largest response. A definitive decomposition of these contributions is left for future work.

Comparing Figures 7 and 8 yields an important design insight. Increasing the Reynolds number does not simply amplify the low-Reynolds-number response; it can also change the preferred harvesting mode. For the density ratio and geometry range considered, the rhombic family covers both bounded oscillation and autorotation, whereas the parallelogram family remains oscillation-dominated. Thus, acute rhombi and the $\lambda = 1.5$ parallelogram remain the preferred choices for oscillation-based harvesting, whereas the

square cylinder is most suitable when continuous rotary output is required.

3.3 Phase-resolved mechanism sustaining bounded oscillation of acute rhombi at low Reynolds number

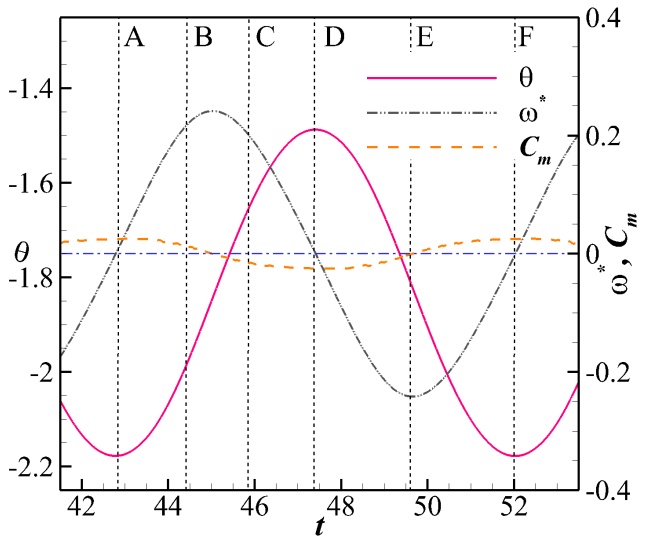

Figure 9. Phase histories of angle θ, angular velocity ω^*, and hydrodynamic moment coefficient C_m for a representative low-Reynolds-number ($Re = 40$) rhombic cylinder. Markers A–F correspond to the wake snapshots in Figure 10.

The foregoing results reveal that, in the low-Reynolds-number conditions, although both rhombic and parallelogram families can sustain bounded oscillation, the acute rhombus with $\alpha = \pi/6$ yields not only the best start-up but also the largest oscillation amplitude, making it the preferred geometry for oscillation-based harvesting under weak-flow conditions. Motivated by this clear advantage, we focus on the $\alpha = \pi/6$ rhombus at $Re = 40$ and conduct a phase-resolved analysis of its rotational dynamics.

To clarify the mechanism by which acute rhombi sustain strong bounded oscillation at low Reynolds number, we examine a representative cycle of the variable-angle rhombic family using the time histories of the rotation angle θ, the dimensionless angular velocity ω^*, and the hydrodynamic moment coefficient C_m, together with the corresponding wake-vorticity fields. Figure 9 shows that the three signals are not in phase but exhibit clear relative phase shifts. The angular velocity is, by definition, the time derivative of the rotation angle and thus leads it by approximately a quarter period for a near-harmonic oscillation, whereas the hydrodynamic moment changes sign near the turning points and reaches its extreme values earlier than ω^*. This phase difference reflects the finite time needed for the separated shear layers and near-body vortical structures to reorganize in response to the instantaneous body orientation.

The time histories over one cycle also reveal how energy is transferred from the flow into the rotational motion. Near the first turning point, the rotation angle is close to its minimum value, the angular velocity is small, and C_m is slightly positive. The positive moment initiates the next half-stroke and accelerates the body toward increasing θ. Over the interval from A to B, C_m and ω^* share the same sign; consequently, the instantaneous hydrodynamic work is positive, and the flow continuously delivers energy to the rotational degree of freedom. As the body moves toward the opposite extreme, the moment weakens and then reverses sign. Around point C, the angular velocity approaches zero while the negative moment acts to restore the body. During the return half-stroke, ω^* is negative, and the negative moment once again aligns with the motion; thus, the flow performs positive work a second time. Therefore, the bounded oscillation is maintained not by a single impulsive event but by two finite time intervals per cycle during which the hydrodynamic moment and the angular velocity remain favorably aligned.

The wake-vorticity snapshots in Figure 10 reveal how this phase relation is established. At instant A, the body is close to a turning point and the near-wake is clearly asymmetric: a compact region of positive vorticity attaches to the lower leeward side, while a region of negative vorticity occupies the upper near wake. This vorticity arrangement generates a positive hydrodynamic moment that initiates the next half-stroke. As the system moves to B, this asymmetry persists, so the hydrodynamic moment remains favorable to increasing θ and the angular velocity continues to grow. By instant C, however, the dominant vortical structures have been convected downstream and reorganized: the positive-vorticity core has moved farther aft, the negative-vorticity lobe has migrated, and the original near-wake asymmetry is weakened. The resulting moment decreases and eventually changes sign, driving the body toward the next turning point.

The transition from C to D is particularly revealing. Once the moment becomes negative, the body accelerates in the reverse direction and attains its largest negative angular velocity. Simultaneously, the

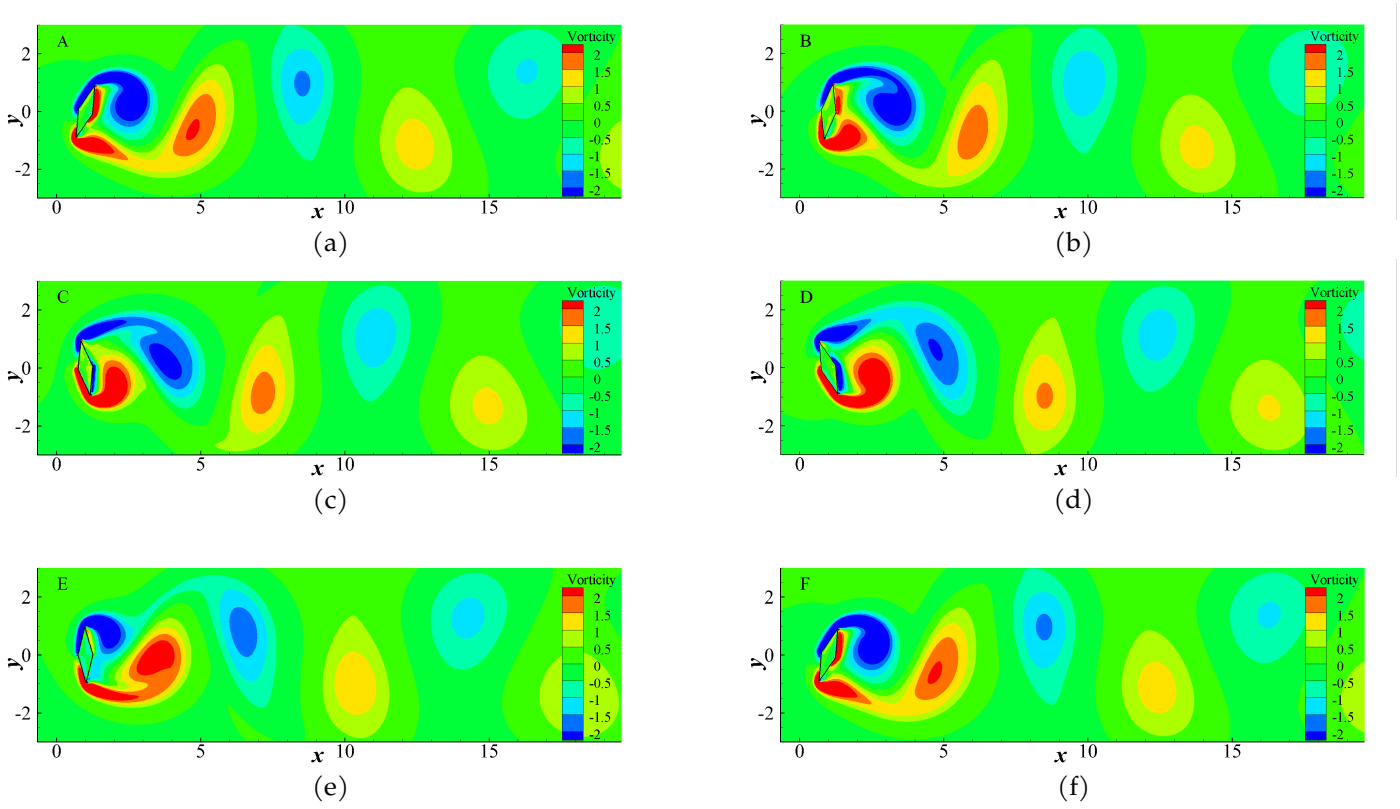

Figure 10. Wake-vorticity fields at six instants A–F, corresponding to panels (a)–(f), for the rhombic cylinder at $Re = 40$, as marked in Figure 9.

wake asymmetry mirrors the earlier A–B configuration but with opposite sign: the dominant vorticity patches reverse their roles on the two sides of the body. Near E, the body approaches the second turning point, the negative moment decays, and the rotation angle reaches its opposite extreme. The subsequent state F closely resembles A, confirming the periodic closure of the cycle. The oscillation is thus sustained by a repeating sequence of near-wake growth, convection, reorganization, and sign reversal of the hydrodynamic moment.

These phase-resolved results demonstrate that the decisive mechanism lies in the local near-wake asymmetry adjacent to the body, rather than in the far wake. For the low-Reynolds-number acute rhombi, sustained bounded oscillation requires that the near-body vortical structures repeatedly re-establish an appropriate asymmetry after each turning point, so that the hydrodynamic moment changes sign at the correct phase of the motion and remains aligned with the angular velocity over finite portions of the cycle. In this sense, the ability of the acute rhombi to maintain strong oscillation is governed not simply by the magnitude of the hydrodynamic moment, but by the correct phase ordering among body motion, moment generation, and near-wake evolution.

4 Conclusions

The vortex-induced rotation of two reconfigurable polygonal harvesting sections — a variable-angle rhombic cylinder and a variable-side-length parallelogram cylinder — has been investigated numerically. The main findings are summarized below.

1. At $Re = 40$, both geometry families remain in bounded oscillatory motion, but their responses are strongly controlled by the geometric parameter. For the rhombic family, decreasing the interior angle systematically improves the start-up response and increases the amplitude of the bounded oscillation, indicating that sharper rhombi are more favorable for oscillation-based harvesting at low Reynolds numbers. For the parallelogram family, the oscillation amplitude varies non-monotonically with the side-length ratio, with the intermediate case $\lambda = 1.1$ producing the largest bounded oscillation.

2. At $Re = 150$, the two geometry families exhibit different response trends. In the

rhombic family, the non-square sections remain on bounded oscillatory branches, and their amplitudes continue to increase as the interior angle decreases. By contrast, the square cylinder ($\alpha = \pi/2$) departs from bounded oscillation and develops autorotation. In the parallelogram family, all cases remain in bounded oscillation, and $\lambda = 1.5$ yields the largest oscillation envelope.

3. Phase-resolved analysis of the rotation angle, angular velocity, hydrodynamic moment coefficient, and wake vorticity reveals the mechanism that sustains the oscillatory response of acute rhombi at low Reynolds number. The bounded oscillation is maintained by the periodic reorganization of near-wake vortical structures, which ensures that the hydrodynamic moment remains favorably aligned with the angular velocity over finite portions of each cycle, thereby allowing the flow to deliver energy continuously into the rotational motion.

Overall, the preferred geometry depends on both Reynolds number and the intended harvesting mode. At low Reynolds number, acute rhombi with small interior angles and the parallelogram with $\lambda = 1.1$ are preferable for start-up and oscillation-based harvesting. At higher Reynolds number, the same acute rhombi and the $\lambda = 1.5$ parallelogram perform best for oscillatory harvesting, whereas the square cylinder becomes the preferred choice for rotary harvesting owing to its autorotation.

Data Availability Statement

The data used to support the findings of this study are available from the corresponding author upon request.

Funding

This work was supported by the National Natural Science Foundation of China under Grant 12372214 and the Fundamental Research Program of Shanxi Province under Grant 202303021221118.

Conflicts of Interest

The authors declare no conflicts of interest.

AI Use Statement

The authors declare that no generative AI was used in the preparation of this manuscript.

Ethical Approval and Consent to Participate

Not applicable.

References

[1] Rostami, A. B., & Armandei, M. (2017). Renewable energy harvesting by vortex-induced motions: Review and benchmarking of technologies. *Renewable and Sustainable Energy Reviews, 70*, 193-214. [CrossRef]

[2] Wang, J., Geng, L., Ding, L., Zhu, H., & Yurchenko, D. (2020). The state-of-the-art review on energy harvesting from flow-induced vibrations. *Applied Energy, 267*, 114902. [CrossRef]

[3] Barrero-Gil, A., Alonso, G., & Sanz-Andres, A. (2010). Energy harvesting from transverse galloping. *Journal of Sound and Vibration, 329*(14), 2873-2883. [CrossRef]

[4] Ibarra, D., Sorribes, F., Alonso, G., & Meseguer, J. (2014). Transverse galloping of two-dimensional bodies having a rhombic cross-section. *Journal of Sound and Vibration, 333*(13), 2855-2865. [CrossRef]

[5] Alonso, G., Meseguer, J., & Pérez-Grande, I. (2007). Galloping stability of triangular cross-sectional bodies: a systematic approach. *Journal of Wind Engineering and Industrial Aerodynamics, 95*(9-11), 928-940. [CrossRef]

[6] Abdelkefi, A., Hajj, M. R., & Nayfeh, A. H. (2012). Power harvesting from transverse galloping of square cylinder. *Nonlinear Dynamics, 70*(2), 1355-1363. [CrossRef]

[7] Abdelkefi, A., Yan, Z., & Hajj, M. R. (2014). Performance analysis of galloping-based piezoaeroelastic energy harvesters with different cross-section geometries. *Journal of Intelligent Material Systems and Structures, 25*(2), 246-256. [CrossRef]

[8] Ding, L., Zhang, L., Wu, C., Mao, X., & Jiang, D. (2015). Flow induced motion and energy harvesting of bluff bodies with different cross sections. *Energy Conversion and Management, 91*, 416-426. [CrossRef]

[9] Zhao, J., Leontini, J. S., Jacono, D. L., & Sheridan, J. (2014). Fluid–structure interaction of a square cylinder at different angles of attack. *Journal of Fluid Mechanics, 747*, 688-721. [CrossRef]

[10] Barrero-Gil, A., Serruys, S., & Velazquez, A. (2022). Influence of cross-section shape on energy harvesting from transverse flow-induced vibrations of bluff bodies. *Journal of Fluid Mechanics, 950*, A25. [CrossRef]

[11] Zhang, B., Mao, Z., Song, B., Ding, W., & Tian, W. (2018). Numerical investigation on effect of damping-ratio and mass-ratio on energy harnessing of a square cylinder in FIM. *Energy, 144*, 218-231. [CrossRef]

[12] Lugt, H. J. (1980). Autorotation of an elliptic cylinder about an axis perpendicular to the flow. *Journal of Fluid Mechanics, 99*(4), 817-840. [CrossRef]

[13] Zaki, T. G., & Gad-El-Hak, M. (1994). Numerical and experimental investigation of flow past a freely

rotatable square cylinder. *Journal of Fluids and structures, 8*(7), 555-582. [CrossRef]

[14] Robertson, I., Li, L., Sherwin, S. J., & Bearman, P. W. (2003). A numerical study of rotational and transverse galloping rectangular bodies. *Journal of fluids and structures, 17*(5), 681-699. [CrossRef]

[15] Ryu, S., & Iaccarino, G. (2017). Vortex-induced rotations of a rigid square cylinder at low Reynolds numbers. *Journal of Fluid Mechanics, 813*, 482-507. [CrossRef]

[16] Ryu, S. (2018). Quadrant analysis on vortex-induced autorotation of a rigid square cylinder. *Journal of Mechanical Science and Technology, 32*(6), 2629-2635. [CrossRef]

[17] Luo, C., Mou, R., Huang, X., Huang, W. X., & Fang, L. (2023). A free-streamline boundary-layer model for small-amplitude oscillation regime of square cylinder under vortex-induced rotation. *Physics of Fluids, 35*(9). [CrossRef]

[18] Wang, H. K., Yan, Y. H., Chen, C. M., Ji, C. N., & Zhai, Q. (2019). Numerical investigation on vortex-induced rotations of a triangular cylinder using an immersed boundary method. *China Ocean Engineering, 33*(6), 723-733. [CrossRef]

[19] Zhu, H., Zhao, Y., & Zhou, T. (2018). Numerical investigation of the vortex-induced vibration of an elliptic cylinder free-to-rotate about its center. *Journal of Fluids and Structures, 83*, 133-155. [CrossRef]

[20] Mou, R. Y., Huang, W. X., Huang, X. R., & Fang, L. (2024). Vortex-induced rotation of a square cylinder under the influence of Reynolds number and density ratio. *Journal of Fluid Mechanics, 986*, A15. [CrossRef]

[21] Fernandes, A. C., & Armandei, M. (2014). Low-head hydropower extraction based on torsional galloping. *Renewable energy, 69*, 447-452. [CrossRef]

[22] Zhang, J., Fang, Z., Shu, C., Zhang, J., Zhang, Q., & Li, C. (2017). A rotational piezoelectric energy harvester for efficient wind energy harvesting. *Sensors and Actuators A: Physical, 262*, 123-129. [CrossRef]

[23] Zhu, H., Chen, Q., Alam, M. M., Tang, T., Zhong, J., & Zhou, T. (2023). Flow-induced rotation and wake characteristics of polygonal prisms subjected to laminar flow. *Physics of Fluids, 35*(5). [CrossRef]

[24] Zhao, M., Zhang, Q., & Liu, Y. (2025). Flow-induced vibration and energy harvesting of an elastically mounted circular cylinder with mechanically coupled rotation. *Journal of Fluid Mechanics, 1021*, A26. [CrossRef]

[25] Huang, W. X., Shin, S. J., & Sung, H. J. (2007). Simulation of flexible filaments in a uniform flow by the immersed boundary method. *Journal of computational physics, 226*(2), 2206-2228. [CrossRef]

[26] Yoon, D. H., Yang, K. S., & Choi, C. B. (2010). Flow past a square cylinder with an angle of incidence. *Physics of fluids, 22*(4). [CrossRef]

[27] Sen, S., Mittal, S., & Biswas, G. (2011). Flow past a square cylinder at low Reynolds numbers. *International Journal for Numerical Methods in Fluids, 67*(9), 1160-1174. [CrossRef]

[28] Park, Y. G., Min, G., Ha, M. Y., & Yoon, H. S. (2015). Response characteristics of vortex around the fixed and freely rotating rectangular cylinder with different width to height ratios. *Progress in Computational Fluid Dynamics, an International Journal, 15*(1), 1-9. [CrossRef]

Ruiyong Mou is with the Research Institute of Aero-Engine, Beihang University, Beijing 100191, China, and also with the BCC Lab, Hangzhou International Innovation Institute of Beihang University. (Email: by2032116@buaa.edu.cn)

Xingrong Huang is with the BCC Lab, Hangzhou International Innovation Institute of Beihang University. (Email: huangxingrong@buaa.edu.cn)

Feng Liu is with the School of Energy and Power Engineering, North University of China, Taiyuan 030051, China. (Email: feng.liu@nuc.edu.cn)